日本磁気学会
ISSN 2432-0250
Journal of the Magnetics Society of Japan
Electronic Journal URL: https://www.jstage.jst.go.jp/browse/msjmag

Vol.43 No.5　2019

Journal

JOURNAL OF THE MAGNETICS SOCIETY OF JAPAN

Vol.43 No.5 2019

日本磁気学会

ISSN 2432-0250

HP: http://www.magnetics.jp/ e-mail: msj@bj.wakwak.com
Electronic Journal: http://www.jstage.jst.go.jp/browse/msjmag

世界初！
高温超電導型VSM

新製品

世界初*、高温超電導マグネットをVSMに採用することで
測定速度 当社従来機1/20を実現。
0.5mm cube磁石のBr, HcJ高精度測定が可能と
なりました。
*2014年7月 東英工業調べ

測定結果例

高温超電導VSMによるNdFeB(sint.) 0.5mm cube BHカーブ

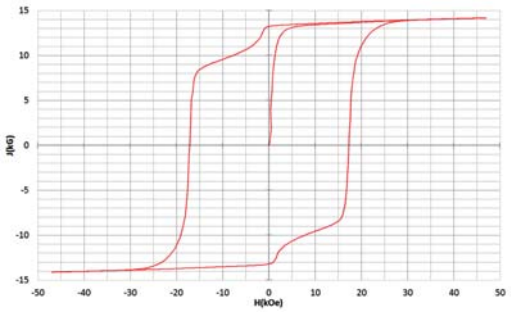

磁化測定レンジ：0.2emu
Br = 13.2kG　　HcJ = 17.2kOe

高温超電導VSMによるNdFeB(sint.) 1mm cube BHカーブ

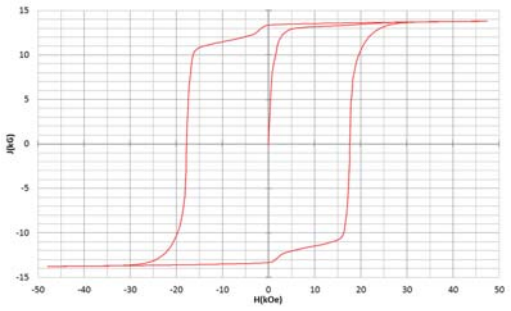

磁化測定レンジ：2emu
Br = 13.3kG　　HcJ = 17.7kOe

高温超電導VSMによるNdFeB(sint.) 4mm cube BHカーブ

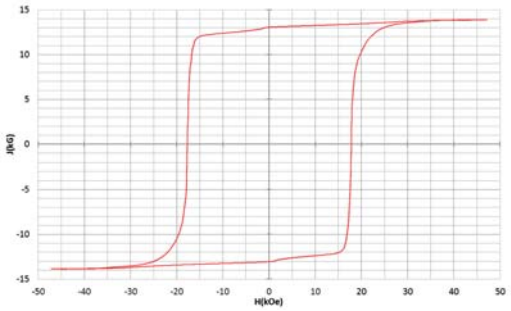

磁化測定レンジ：100emu
Br = 13.1kG　　HcJ = 17.8kOe

高速測定を実現

高温超電導マグネット採用により、高速測定を実現しました。Hmax= 5Tesla, Full Loop 測定が2分で可能です。
（当社従来機：Full Loop測定　40分）

小試料のBr,HcJ高精度測定

0.5mm cube 磁石のBr,HcJ高精度測定ができ、表面改質領域を切り出しBr,HcJの強度分布等、微小変化量の比較測定が可能です。
また、試料の加工劣化の比較測定が可能です。

試料温度可変測定

−50℃～+200℃温度可変UNIT（オプション）

磁界発生部の小型化

マグネットシステム部寸法：0.8m×0.3m×0.3m

TOEI 東英工業株式会社
http://www.toeikogyo.co.jp
〒194-0035 東京都町田市忠生1-8-13
TEL：042-791-1211　FAX：042-792-0490
E-mail : sales@toeikogyo.co.jp

有限要素法解析ソフトウェア COMSOL Multiphysics®

COMSOL MULTIPHYSICS®

マルチフィジックスの進化論

無制限・強連成で実現象に即したシミュレーション事例のご紹介

永久磁石を利用した磁気軸受の解析例

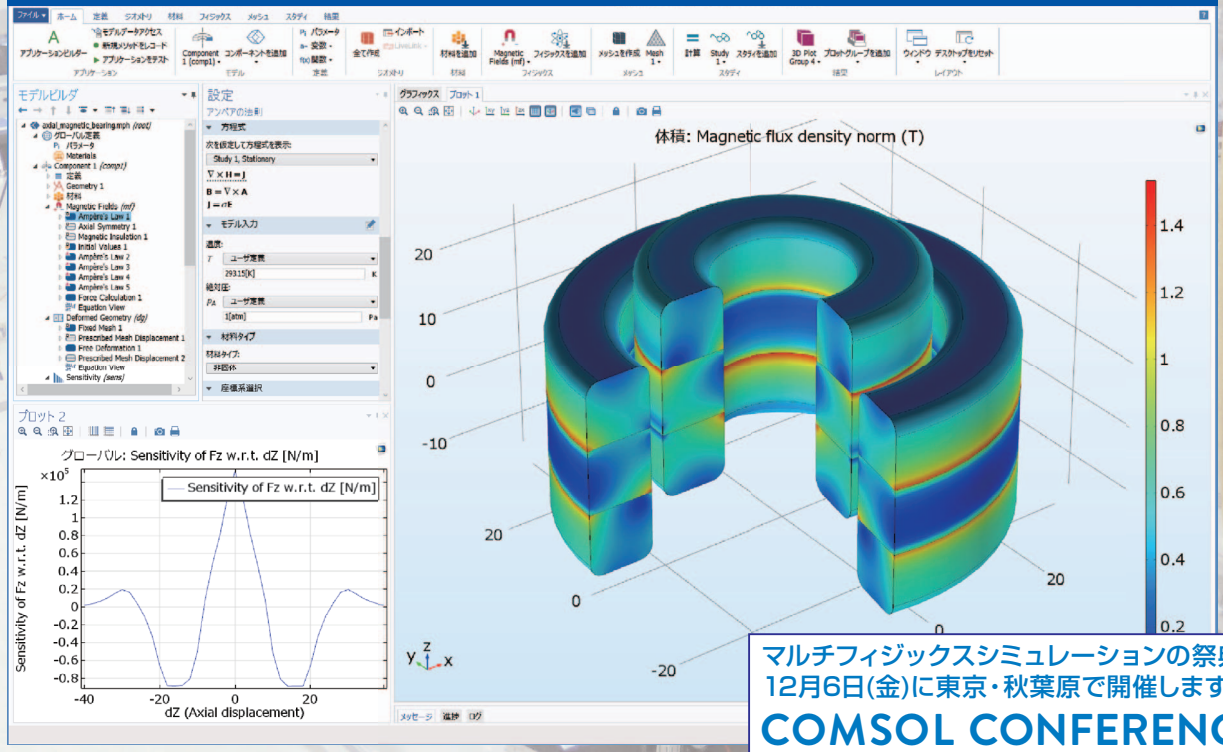

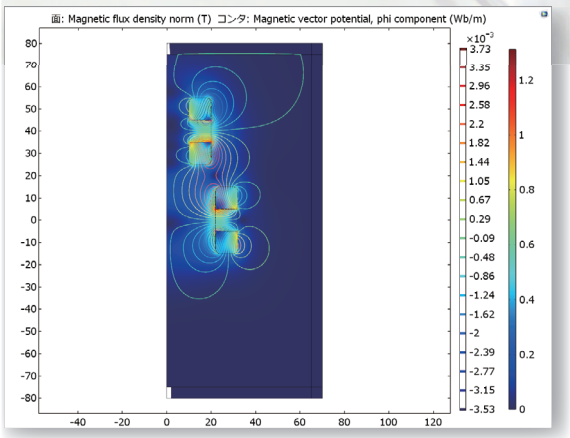

AC/DC モジュールの適用例

- AC/DC 電流分布、電場分布
- バイオヒーティング
- コイルとソレノイド
- SPICE 回路とフィールドシミュレーション
- 接触抵抗
- 電磁両立性 (EMC) および電磁妨害 (EMI)
- 電磁力およびトルク
- 電磁力シールド
- 電気機械の変形
- ホール効果を利用したセンサ
- インシュレータ、コンデンサ、誘電体
- モータ、ジェネレータ、および他の電気機械
- 非線形材料
- 寄生容量とインダクタンス
- 永久磁石と電磁石
- 多孔質材料
- 抵抗および誘導加熱
- センサ
- 超伝導体
- 変圧器とインダクタ

永久磁石を使用した磁気軸受の解析例

永久磁石を使用した軸受はターボ機械、ポンプ、モータ、発電機やフライホイール式エネルギー貯蔵システムなど、様々な分野で使用されています。非接触かつ潤滑不要で保守整備を大幅に省略できる点は、従来の機械式ベアリングと比べて重要なメリットです。
この例では、軸方向の永久磁石軸受の磁気力と剛性などの設計パラメータを計算する方法を示しています。

※AC/DCモジュールはCOMSOL Multiphysics®と併用するアドオン製品です。

COMSOL Multiphysics® なら、今まで不可能だった 3 種以上のマルチフィジックス解析を強連成で実現できます。30 日間全機能無料トライアル、無料の導入セミナー、1000種を超える世界の様々な事例をご提供いたします。詳しくは、下記の弊社営業部までお問い合せください。

COMSOL
http://www.comsol.jp

KESCO KEISOKU ENGINEERING SYSTEM
計測エンジニアリングシステム株式会社
https://kesco.co.jp/service/comsol/
Tel : 03-5282-7040 ・ Fax : 03-5282-0808

Journal of the Magnetics Society of Japan
Vol. 43, No. 5

Electronic Journal URL: https://www.jstage.jst.go.jp/browse/msjmag

CONTENTS

J. Magn. Soc. Jpn., **43**, 91-98 (2019)

<Paper>

Permeability Measurement up to 30 GHz of a Magnetically Isotropic Thin Film Using a Short-Circuited Coaxial Line

S. Takeda*,***, H. Kijima-Aoki**, H. Masumoto**, and H. Suzuki***

*Magnontech Ltd., *787-16 Jurokken, Kumagaya, Saitama 360-0846, Japan*

**Frontier Research Institute for Interdisciplinary Science, Tohoku University, *Sendai, 980-8578, Japan*

***KEYCOM Corp., *3-39-14, Minami Ohtsuka, Toshima-ku, Tokyo 170-0005, Japan*

In this study, the high frequency permeability (μ) and ferromagnetic resonance(FMR) phenomena of a thin film with a strong perpendicular magnetic anisotropy and in-plane magnetically isotropic properties was measured using the short-circuited coaxial line technique; the analyzed sample had a toroidal shape. A field method was used for the background correction, where a strong magnetic bias field was applied and removed. However, when using a short-circuited coaxial line, the μ=1 condition cannot be achieved beyond a few ten GHz frequencies, whereas ferromagnetic resonance (denoted as FMR2) occurred because of the insufficient bias field. This resonance was compensated using the Landau-Lifshitz-Gilbert (LLG) equation, and the net μ-f properties without the bias field (denoted as FMR1) up to 30 GHz successfully extracted. Finally, a good agreement between the experimental results and the calculations based on the assumption of a magnetic multi-domain structure in FMR1 was achieved.

Keywords: magnetic thin film, perpendicular anisotropy, ferromagnetic resonance, FMR, LLG, permeability measurement, GHz band, short-circuited coaxial line, wideband measurement

1. Introduction

Nowadays, the development of wireless local area network, car collision avoidance radar, and automatic car driving test system, among others, has led to the application of magnetic materials at several 10 GHz bands. With this trend, the demand for measuring the high frequency permeability of magnetic thin films in this band region has been increasing accordingly.

We have already reported such measurement results for the 10-30 GHz band using short-circuited microstrip line test fixtures. [1, 2] Improving the present fixtures is crucial for performing measurements at higher frequencies. On the other hand, a short-circuited coaxial line can also be used, without the need to consider the external noise due to a perfectly shielded structure. Furthermore, the output connector of the vector network analyzer (VNA) is always coaxial, avoiding drastic mode changes and allowing the suppression of a higher-order wave. Because of this structural advantage, the permittivity (ε) and permeability (μ) of bulk materials have been investigated in several studies [3,4] by measuring the transmitted and reflected waves simultaneously.

However, these simultaneous measurements can generate some errors, the method is not suitable for materials with large frequency dispersions of ε and μ, and there are no reports on permeability measurements based on the short-circuited coaxial line technique, which is the topic of this study.

Amorphous Co–Zr–Nb films and Fe–Ni films with uniaxial anisotropy are typical magnetic thin films exhibiting high permeability at high frequencies, but their natural resonant frequencies are limited to few-gigahertz bands. In our group, nanogranular films with a higher natural resonant frequency were prepared by sputtering[5,6,7,8]. In this study, a $Co_{52}(SiO_2)_{48}$ film was selected as the target material because (1) it has a higher resonant frequency above 10 GHz and (2) it is in-plane isotropic, which is favorable for a coaxial line with a rotational symmetry.

The lumped-element approximation of a short-circuited transmission line and the field method are usually adopted for the zero correction. The latter requires the μ = 1 condition for the sample which is obtained by applying a strong external bias magnetic field. However, this condition cannot be achieved for the coaxial line because the bias magnetic field is straight-line-like and the microwave field is circular-like, so that some parts certainly cross between both of them. Here we also discuss the problems of applying the field method to the coaxial line configuration.

2. Measurement Procedure

2.1. Test fixture

Figure 1 displays a schematic cross sectional view of our short-circuited coaxial line test fixture with a mounted sample. A 5 mm straight line is connected to the transform adaptor between the Sub Miniature Type A (SMA) and the Amphenol Precision Connector-7 mm (APC-7) connectors. Figure 2 shows the time-domain reflectometry characteristics of the test fixture without sample; the characteristic impedance is kept within 50 ± 1 Ω until the short end.

The rated upper limited frequency of an APC-7 connector is 18 GHz, and the commercial calibration kit could not be used. Hence, we realized an open-short-load calibration kit for up to 30 GHz. The reference plane for calibration is the APC-7 side of the transform adaptor, as shown in Fig.1.

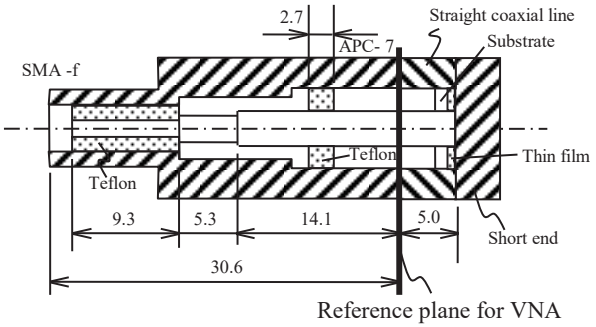

Fig. 1 Cross section of the short-circuited coaxial fixture loading a toroidal shaped thin film sample.

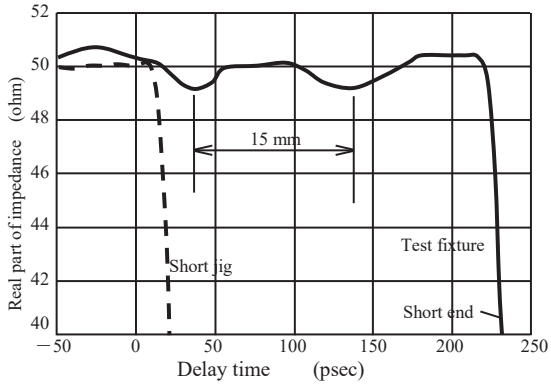

Fig.2 TDR characteristics of the short-circuited coaxial test fixture without the sample.

The magnetic toroidal-shaped thin film, with 1.5 μm thickness, deposited on a 0.5 mm thick glass substrate (Fig. 3), is loaded at the short end. The sample is mounted so that the film comes into contact with the short end and the substrate faces the microwave source side, as shown in Fig. 4.

When thickness d = 0.5 mm and permittivity ε = 6 of the substrate, the electric length is $d\varepsilon^{0.5}$ = 1.22 mm that is less than half of $\lambda/4$ = 2.5 mm where λ is free space wavelength of 30 GHz. So, the lumped-element approximation enough holds.

2.2. Field method

Permeability can be derived from the reflection parameter (S_{11}) measured with the VNA using the short-circuited coaxial line.

First, a glass substrate without a magnetic thin film is inserted into the test fixture, an external strong bias magnetic field is applied, and S_{11} is measured. After removing the bias magnetic field, S_{11} is measured again.

The background signal is calculated and converted into equivalent permeability from both of S_{11} signals. This signal doesn't involve the influence by the substrate's permittivity. However, since Ni plating is used in the transform adaptor, the background signal is very large.

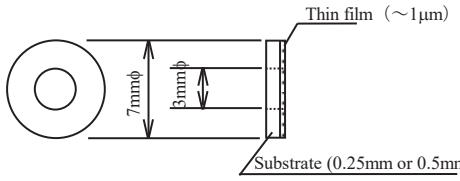

Fig. 3 Front and cross sectional views of the magnetic toroid-shaped thin film on a glass substrate.

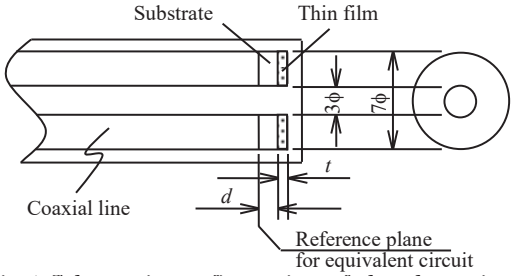

Fig.4 Schematic configuration of the short-circuited coaxial line and the magnetic toroid-shaped thin film sample

Second, the substrate coated with the magnetic thin film is inserted into the coaxial line. Two S_{11} values are measured, with and without strong bias magnetic field, which is applied in-plane of the thin film. This procedure allows the detection of the signal that carrying the information about the permeability of the magnetic thin film.

Finally, a signal related to this μ can be picked out by subtracting the abovementioned background signal from a signal including the magnetic permeability of this film.

3. Effective Permeability Evaluation

3.1. Lumped-element approximation

In general, when a measurement angular frequency is $\omega = 2\pi f$, the input admittance (Y) of the short-circuited transmission line with electrical length l, filled with a medium having μ and ε, is expressed as follows;

$$Y = 1/(j\omega\mu L\, l) + (1.15/3)j\omega\varepsilon C\, l, \quad (1)$$

where, L = 166.9 nH/m and C = 66.67 pF/m are the inductance and capacitance per unit length of 50 Ω transmission line in the air.

Equation (1) is applicable to both partially and uniformly filled cases. In the former case, the effective permeability (μ_e) and permittivity (ε_e) are used instead of μ and ε. The equation holds within ±5 % error range until $(2\pi(\varepsilon_e\mu_e)^{0.5}/\lambda)\, l = 1.4$ rad. [9]

Here, we introduce new parameters:

$$L_o = L\, l,\ C_o = (1.15/3)\, C\, l. \quad (2)$$

Hence, Eq. (1) can be rewritten as follows:

$$Y_o = 1/(j\omega\mu L_o) + j\omega\varepsilon C_o, \quad (3)$$

meaning that the equivalent circuit is a parallel L_oC_o circuit, as shown in Fig.5.

The reference plane to analyze is placed on the substrate surface, where the microwave impinges. Therefore, l is given by the sum of the thickness of

substrate (d) and the magnetic thin film (t): however, when the latter is ignored, $l = d$. When the imaginary part ε_e" of the effective complex permittivity of the substrate is so small to be negligible, C_o becomes $C_s = \varepsilon' C_o$ as shown in Fig. 6(a).

3.2. Determination of C_s and the coupling coefficient

The substrate permittivity of $\varepsilon = 6$, measured by a different way, was used to calculate $C_s = \varepsilon C_o$.

The coupling coefficient (η), which is the ratio between the thin magnetic film volume and the whole volume of a toroidal sample, is given by

$$\eta = t/(d+t) \cong t/d = 0.0015/0.5 = 0.03. \quad (4)$$

Its value is very small but can be obtained relatively correctly, allowing also the absolute value measurement. In our study, $d = 0.5$ mm and $t = 1.5$ μm were used.

3.3. Derivation of the effective permeability $\mu_e' - j\mu_e''$

The effective magnetic permeability is derived using the field method from the input admittances for the equivalent circuits shown in figures. 6 and 7 in the usual way: please refer to previous papers[1,9,10,11] for details.

Attention should be paid to the use of magnetic materials in the transform adaptor between SMA and APC-7, so the magnetic signal is observed by the field method even in an empty fixture. When both substrates without and with the magnetic thin film are individually loaded into the fixture, the each signal contains also this magnetic signal. The signal from the magnetic thin film alone is obtained by subtracting the substrate one from that of the film-substrate system; this procedure can be described using numerical formulas.

First, when considering the background effective complex permeability $\mu_b = \mu_b' - j\mu_b''$, L_o becomes $\mu_b' L_o$ and the series resistance $\omega\mu_b'' L_o$ is introduced, as shown in Fig. 6(a). When a strong bias magnetic field H_{ext} is applied to this, the effective magnetic permeability changes into $\mu_{bo} = \mu_{bo}' - j\mu_{bo}''$, corresponding to what is shown in Fig. 6(b). The effective susceptibility ($\mu_b - \mu_{bo}$) is obtained by comparing the measured input admittances for the two circuits of Fig. 6.

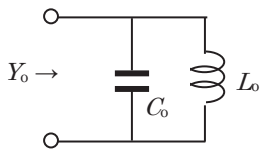

Fig. 5 Equivalent circuit of coaxial test fixture.

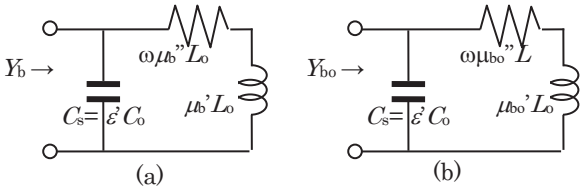

Fig. 6 Equivalent circuits for the glass substrate without the sample and loaded in the test fixture, (a) without and (b) with the bias magnetic field.

Next, when considering the glass substrate coated with the magnetic thin film, the whole effective permeability is given by the sum of the background effective permeability and the thin film permeability: $\mu_b + \mu_f$. When applying a strong bias magnetic field, this becomes $\mu_{bo} + \mu_{fo}$. These two cases are represented in Fig. 7(a) and (b), respectively. The effective susceptibility, that is, $(\mu_b + \mu_f) - (\mu_{bo} + \mu_{fo})$ is obtained by comparing both admittances.

The subtraction of the results of Fig. 6 from those for Fig. 7 leads to $1+\chi$, and, consequently, to

$$1 + \chi = 1 + (\mu_b + \mu_f) - (\mu_{bo} + \mu_{fo}) - (\mu_b - \mu_{bo}) = 1 + \mu_f - \mu_{fo} = 1 + \mu_f' - \mu_{fo}' - j(\mu_f'' - \mu_{fo}''), \quad (5)$$

where $1+\chi$ is the measured permeability. This corresponds to the vertical axis of Fig.12.

The effective permeability $1 + (\mu_f - \mu_{fo})$ of the magnetic thin film can be picked out. The condition of $\mu_{fo} = 1$ is realized in the usual field method, so that $\mu_f = 1 + \chi$, allowing the μ_f calculation.

However, the $\mu_{fo} = 1$ condition can be avoided for the following reason. The direction of the microwave magnetic field (h_{rf}) to the bias magnetic field (H_{ext}) in the field method for a toroidal sample is considered, as shown in Fig. 8. The microwave magnetic field acts uniformly along the circumference direction inside the toroidal-shaped sample, whereas H_{ext} acts along the one-way straight one, as shown in Fig. 8. Therefore, H_{ext} is parallel or antiparallel to h_{rf} on a' and c' parts, so that the signals from those parts are rarely detected.

On the other hand, both fields are normal on the b' and d' parts, and this partial signal is clearly detected.

As in this experiment, the thin film does not saturate even if a magnetic field of $H_{ext} = 5240$ Oe is applied. On the contrary, the ferromagnetic resonance occurs by H_{ext} around 24 GHz. At that frequency, the value of μ_f" becomes very large due to the resonance so the imaginary part ($\mu_f'' - \mu_{fo}''$) of the equation (5) is observed as negative because μ_f" is almost zero.

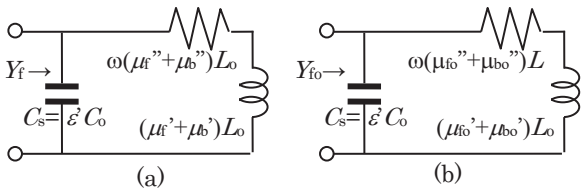

Fig. 7 Equivalent circuits for the magnetic thin film loaded in the test fixture, (a) without and (b) with the bias magnetic field.

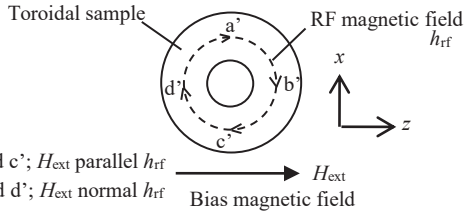

Fig. 8 Schematic of bias magnetic field and RF magnetic field in a toroidal sample.

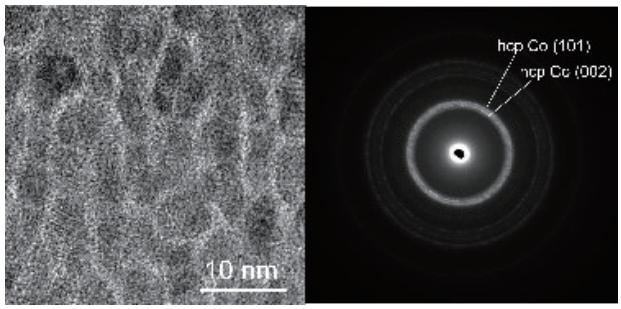

Fig. 9 Cross-sectional image and diffraction pattern of Co_{52}–$(SiO_2)_{48}$

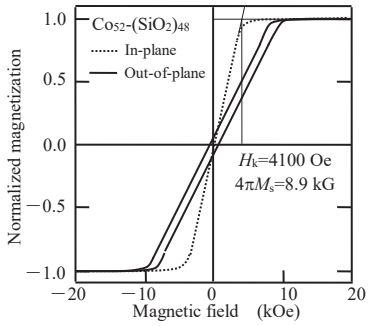

Fig. 10 Magnetization curve of Co_{52}–$(SiO_2)_{48}$ magnetic thin film.

4. Magnetic Thin Film Preparation

A nanogranular film of Co_{52}–$(SiO_2)_{48}$ was fabricated using the radiofrequency (RF) magnetron sputtering method with the conditions[8]: the targets of Co chips (5 × 5 mm) and SiO_2 (ϕ50 mm), the input power of 200 W, in the atmosphere of Ar gas (pressure 0.22 Pa).

The fabricated film's crystalline structure and organization were determined using transmission electron microscopy energy dispersive spectroscopy. As shown in Fig. 9, the structure consisted of a slender Co grains with 3-5 nm diameter and 5-10 nm length, arranged normal to plane in amorphous SiO_2 matrix: these phases appeared as separate, and Co exhibited a random-hexagonal-closed- packed structure.

The static B-H curve was measured in a vibrating sample magnetometer. The magnetization curve is shown in Fig. 10; its shape remained unchanged even when the direction of the static magnetic field was changed in the plane. From the in-plane magnetization curve, saturation magnetization $4\pi M_s$ and perpendicular magnetic anisotropy field H_k were decided to be 8.9 kG and 4.1 kOe , respectively. The coercivity of a hysteresis perpendicular to the film plane was about 210 Oe, which is quite smaller than that of the hard magnetic film.

5. Results and Discussion

5.1. Bias magnetic field influence on the background

The experimental results of the effective complex permeability for the glass substrate in the short-circuited coaxial line, alone and coated with the thin film, are shown in Fig. 11.

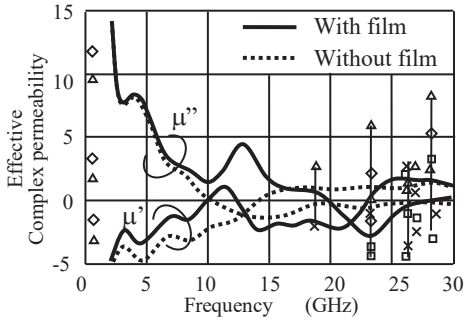

Fig. 11 Frequency dependences of effective complex permeability, $1+(\mu_b+\mu_f)-(\mu_{bo}+\mu_{fo})$ of the substrate with film and $1+(\mu_b-\mu_{bo})$ of it without film.

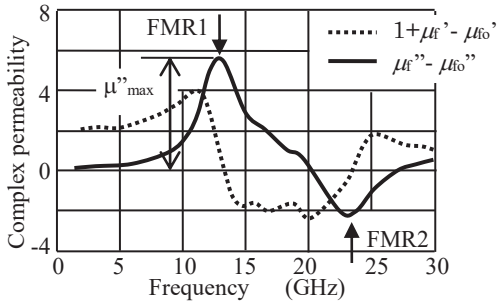

Fig. 12 Measured μ-f curve of magnetic film with 1.5 μm thickness on 0.50 mm$t$ substrate by the field method (5.2kOe)

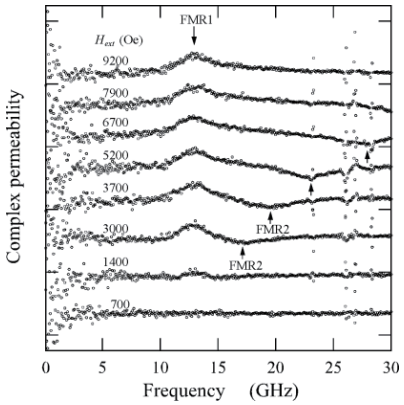

Fig. 13 Measured μ-f curve of magnetic thin film with 1.5 μm thickness on 0.50 mm$t$ substrate using field method with various H_{ext} of 700-9200 Oe.

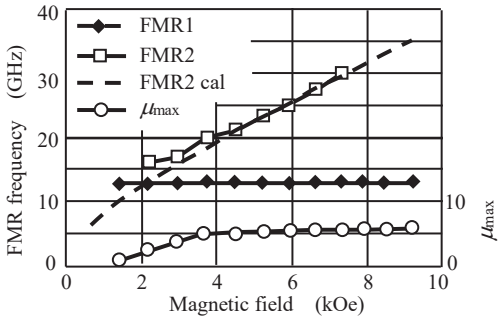

Fig. 14 Field dependences of the FMR frequencies and the maximum imaginary value $\mu"_{max}$ of FMR1.

Both bias magnetic fields were 5.2 kOe in the field method, with the dashed lines corresponding to μ_{bo}, and the solid lines corresponding to $\mu_b + \mu_f$. Both permeability values at 2GHz increases more than ten times compared to those of at 10 GHz, probably because the magnetic property of the transform adaptor between SMA and APC-7 was detected. Very large background signal were recorded, but a little difference was observed when expanding the magnification beyond 2 GHz, which is our objective signal of the magnetic thin film. Four spike-like noises (at 19, 23, 26.5, and 28 GHz) were observed.

The rated frequency of APC-7 is 18GHz, which relates to the cutoff frequency f_c of TE_{11} mode as a higher harmonic and is given as follows [12]:

$$f_c = (c/2\pi)\{2/(a+b)\} \quad (6)$$

where, c is the speed of light, and a and b are the inner and outer diameters, respectively, of the coaxial line.

The f_c is calculated as 19 GHz for APC-7, which corresponds to the first spike noise in Fig. 11.

Hereinafter, these spike-like noises will be omitted from permeability profile.

Figure 12 shows the results of subtracting the signals of the glass substrate alone from those of the one coated with the magnetic thin film, which correspond to the permeability signals of the latter that were detected with a relatively low noise in spite of a large background signal.

A resonant peak (denoted as FMR1), looking like natural resonance, was observed at around 13 GHz, but a large minus peak of μ" (FMR2) was also observed at 24 GHz.

In the measurement principle of the adopted field method, the state applied by the strong bias magnetic field is assumed to be the reference state ($\mu = 1$); hence, in case of some absorption in this state, μ" is observed as a minus. This phenomenon corresponds to the minus value of μ_f" $-\mu_{fo}$" in case of μ_{fo}" > μ_f" in the equation (5).

Then, the maximum μ" of FMR1 was denoted as $\mu"_{max}$, and we examined how its value was influenced by the H_{ext} strength.

Changes in the μ"-f property of the film by H_{ext} with 700–9200 Oe are indicated in Fig. 13. Both the FMR1 and FMR2 peaks appeared at 3 kOe, and the resonant frequency of FMR2 linearly increased with the H_{ext} strength.

5.2. Derivation of the anisotropic field H_k of the thin film at a high frequency

The results shown in Fig. 13 are plotted in Fig. 14; the resonant frequency of 13 GH of FMR1 remained unchanged even when the magnetic field strength was changed. As discussed in detail in Section 5.3, FMR1 was definitely regarded as natural resonance of the thin film. Its maximum $\mu"_{max}$ value increased straightforwardly and became constant at about 4.1 kOe which corresponds to the saturation by the bias magnetic field.

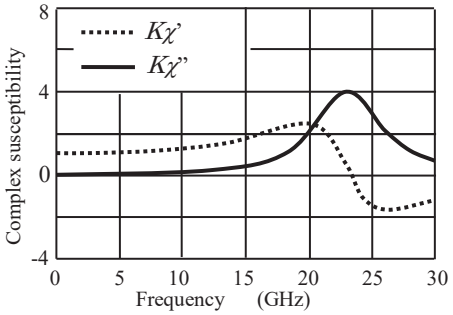

Fig. 15 Calculated $K\chi$-f curve (FMR2) for the subtraction from Fig. 12.

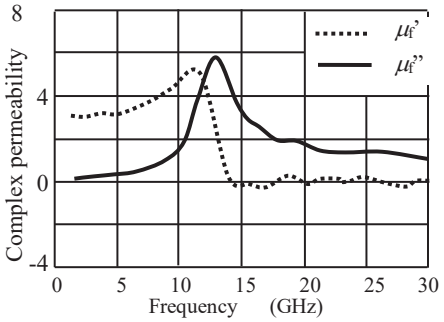

Fig. 16 Subtracted μ-f curve (FMR1) of Fig. 15 from Fig. 12.

The main concern was the magnetic field dependence of FMR2. This peak appeared at 1.5 GHz and H_{ext} = ~2.2 kOe; and when the magnetic field strength was increased, it moved monotonously toward the high frequency side. It was detected mostly at the b' and d' parts shown in Fig. 8 and corresponds to the FMR by the bias magnetic field.

The resonance frequency (f_r) of FMR2 is given as follows [13] (see the Appendix).

$$f_r = (\gamma/2\pi)\{H_{ext}(H_{ext} - H_k + 4\pi M_s)\}^{1/2} \quad (7).$$

The curve calculated on the basis of this equation, which well agreed with the measured frequency dependence of FMR2, is plotted as a dotted line in Fig. 14. In this case, $4\pi M_s$ = 8.9 kG、H_k = 3.4 kOe, and ($\gamma/2\pi$) = 3.1 GHz/kOe (g = 2.21) were used; this H_k is smaller than that derived from the static magnetization curve (4.1 kOe) shown in Fig. 10. The value of H_k = 3.4 kOe was used for the following analysis.

5.3. Calculation of the μ-f curve of FMR2

The film saturated by the bias magnetic field had a single domain structure magnetized in-plane. In this case, an FMR curve can be calculated by the following equation derived from the Landau-Lifshitz-Gilbert (LLG) formula. It is defined that the x-axis is parallel to the microwave magnetic field in the film plane, which is perpendicular to the z-axis of the bias magnetic field in the film plane, the y axis was vertical to the film plane.

Then, the demagnetization factor can be expressed as $N_x = N_z = 0$ and $N_y = 1 - H_k/4\pi M_s$ (see the Appendix). The

perpendicular magnetic anisotropy field H_k reduced N_y.

$$\chi' = \mu_{xx}' - 1 = \omega_m[A_y\{A_xA_y - \omega^2(1+\alpha^{2)}\} + (\omega\alpha)^2(A_x + A_y)]/CC^* \quad (8a),$$

$$\chi'' = \mu_{xx}'' = \omega_m\omega\alpha[\omega^2(1+\alpha^{2)} + A_y^2]/CC^* \quad (8b),$$

where

$$CC^* = [A_xA_y - \omega^2(1+\alpha^{2)}]^2 + [\omega\alpha(A_x + A_y)]^2 \quad (8c),$$

$\omega_m = \gamma 4\pi M_s$, α is the Gilbert relaxation coefficient, $A_x = \omega_e$, $A_y = \omega_e - \omega_k + \omega_m$, and

$$\omega_e = \gamma H_{ext},\ \omega_k = \gamma H_k \quad (9).$$

A magnification factor of K was introduced as $K\chi'$ and $K\chi''$, where the K means that the volume ratio of the magnetic film contributes to the permeability signal. Theoretically, the surface integral of the x-component of the high frequency magnetization shown in Fig. 8 led to $K = 2/\pi = 0.64$.

The calculated complex susceptibility $K\chi'$ and $K\chi''$ are shown in Fig. 15; $4\pi M_s$ = 8.9 kG, α = 0.11, H_{ext} = 5.24 kOe, H_k = 3.4 kOe and K = 0.47 were used.

In Fig. 16, the corrected μ-f curve is plotted that the measured μ in Fig.12, compensated by the calculated μ of FMR2 in Fig.15. FMR2 disappeared and the μ' and μ'' values below 15 GHz rose a little. To confirm the validity of this correction (Fig.16), we measured μ-f by using Field method with application of maximum H_{ext} up to 9.2 kOe and obtained similar to those shown in Fig. 16.

5.4. Calculation of the μ-f curve of FMR1

Next, we discusse how the result for FMR1 shown in Fig. 16 can be explained using an LLG equation.

The magnetic domain structure of the remaining magnetization state was considered for FMR1. The state of the vertical magnetization cannot exist as a single magnetic domain and always has numerous magnetic domain structures repeated alternatively. We assumed a periodic checkered magnetic domain structure, as shown in Fig. 18(b).

This periodic structure can be represented by one magnetic domain, if the magnetic circumstances surrounding one domain could be considered. Equations (8a) and 8(b) can be used in the same way. Then, we assumed that the z-axis was vertical to the film plane and parallel to H_k, the x-axis was parallel to h_{rf} in-plane, and the y-axis was normal to the x-axis in-plane.

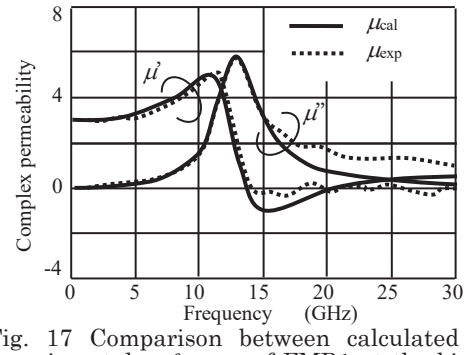

Fig. 17 Comparison between calculated and the experimental μ-f curve of FMR1 at the bias field of 5.2kOe.

If the magnetic domain size is sufficiently small, the demagnetization field will not appear along the z-axis and we will have $N_z = 0$.

The in-plane demagnetization field is strongly influenced by the neighboring magnetic domain. The x-direction component of the high frequency magnetization synchronizes with h_{rf} so that the magnetic charge does not appear on the magnetic domain wall (y-z plane), and we have $N_x = 0$.

The demagnetization field along the y-direction was an issue. A large magnetic charge appeared on the domain wall (z-x plane) because of the Smit and Wijn effect [14] and introduced a large demagnetization field. We had to estimate a large N_y because it would have allowed the calculation of the μ-f curves of the remaining magnetization. Here, we had to substitute H_k with H_{ext} in Eq. (9).

Figure 17 shows the results calculated using $4\pi M_s$ = 8.9 kG, α = 0.16, $N_x = N_z = 0$, N_y = 0.21, $H_k = H_{ext}$ = 3.4 kOe, and K = 0.72. The theoretically calculated K value was K = 1 in the isotropic structure. The experimental results shown in Fig. 17 are also represented as a dashed line in the same figure for comparison, while the high- and low-band noises were omitted.

The compared results well agreed below the natural resonance frequency of 13 GHz. When a measurement error was considered, they also qualitatively agreed at frequencies higher than 15 GHz. However, when comparing them precisely, a discrepancy was observed since μ'' did not approach zero at higher frequencies, as predicted by the calculation.

However, this phenomenon is physically reasonable. Magnetostatic and spin waves are easily excited as a higher mode because the supplied microwave energy has a high level and, reflecting this influence, the loss increases at bands higher than resonant frequency. This phenomenon is usually observed in FMR experiments.

Thus, the saturation magnetization, the anisotropic magnetic field, and the bias magnetic field can help quantitatively explain the magnetic behavior of the

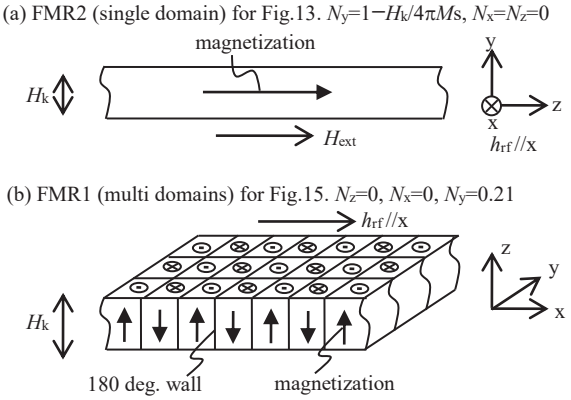

Fig. 18 Schematic domain structures of thin film with perpendicular magnetic anisotropy. (a) with and (b) without bias magnetic field.

Table 1 Comparison between natural resonance (FMR1) and compulsory FMR (FMR2).

		FMR1	FMR2
$4\pi M_s$ (kG)		8.9	8.9
H_k (kOe)		3.4	3.4
Demagnetization factor	N_x	0	0
	N_y	0.21	$1-H_k/4\pi Ms$
	N_z	0	0
Magnification factor K (Theoretical value)		0.72 (1)	0.47 (0.64)
Relaxation factor α		0.16	0.11
Resonance		Natural	Ferromagnetic

prepared thin film near 30 GHz using values from other experiments.

The compulsory ferromagnetic resonance (FMR) phenomenon FMR2 due to the bias magnetic field, beside the natural resonance FMR1 of the thin film material, was observed using this experiment method. As a result, we could specify the FMR relaxation coefficient α.

The analytical method discussed here contains substantial information, natural resonance and ferromagnetic resonance, and is expected to expand its application area more.

6. Conclusion

In this study, we measured the magnetic permeability up to 30 GHz of an in-plane isotropic nanogranular thin film with perpendicular magnetic anisotropy using a short-circuited coaxial line test fixture. The specimen's geometry was toroidal.

A field method was used for the zero correction: a strong external bias magnetic field was applied to ensure the μ=1 condition. However, this condition was not achieved in the short-circuited coaxial line. In addition to the natural resonance of the magnetic thin film, a compulsory FMR phenomenon caused by the bias magnetic field was also observed.

We contrived how to compensate the FMR by calculating the susceptibility, taking the perpendicular anisotropy field into account. This calculations process was carried out on the basis of the phenomenological theory of FMR (i.e., the LLG equation); the FMR relaxation coefficient could also be derived by fitting the experimental results to the theoretical curve.

The FMR1 and FMR2 results are summarized in Table 1. The relaxation coefficient of FMR2 was quite smaller than that of FMR1. The K factor was not 0.64 for FMR2, but the K_{FMR2}/K_{FMR1} ratio became 0.47/0.72 = 0.65, which closely resembles 0.64. If about 70 % of the whole thin magnetic film acted along the theoretical prediction, this agreement makes sense, thereby, insisting the justice of our analytical way.

From the abovementioned results, we can conclude that the high frequency magnetic permeability of the prepared thin film with perpendicular magnetic anisotropy was measured within a frequency band up to 30 GHz using a short-circuited coaxial line and considering the magnetic field strength for the zero correction and the film magnetic parameters.

However, this analytical way is restricted to the area where the condition of a single magnetic domain should be required when applying a strong bias magnetic field. Materials with a high magnetic coercive force cannot be analyzed, whereas soft magnetic thin films allow FMR experiments even at a frequency as high as 30 GHz.

Appendix

Resonance condition and complex susceptibility of an in-plane magnetized thin film having perpendicular anisotropy [13]

In general, the complex susceptibility $\chi = \chi' - j\chi''$ and the resonance condition of a magnetic thin film, magnetized along the z-axis by H_{ext} and excited by h_{rf} along the x-axis, are expressed as same as Eq.(8a), (8b), and (8c).

The resonance condition is achieved when Eq. (8c) becomes minimum, where $\alpha = 0$ leads to Eq. (8c) = 0, resulting the next equation:

$$\omega^2 = A_x A_y = \{\omega_e + (N_x - N_z)\omega_m\}\{\omega_e + (N_y - N_z)\omega_m\} \quad (A1)$$

In case of a film without magnetic anisotropy, $N_x = N_z = 0$, $N_y = 1$, and the resonance condition is

$$\omega^2 = \omega_e(\omega_e + \omega_m). \quad (A2)$$

The coordinate axes are shown in Fig.A-1.

The film system including the perpendicular anisotropic constant K_u, shown in Fig.A-2, possesses magnetic free energy that is expressed as follows:

$$E = -(1/2)4\pi M_s H_{eff} + K_u \cos^2\theta, \quad (A3)$$

where θ is the angle slightly deviated from the z-axis.

H_{eff} is the demagnetizing field expressed as $H_{eff} = -N_y 4\pi M_s \sin\theta$.

Eventually, the free energy becomes

$$E = (1/2)(4\pi M_s)^2 [N_y - (2K_u/(4\pi M_s)^2]\sin^2\theta. \quad (A4)$$

When N_y=1, the effective demagnetization factor N_{ye} along the y-direction can be written as follows:

$$N_{ye} = 1 - H_k/(4\pi M_s) \quad (A5)$$

$$H_k = 2K_u/4\pi M_s \quad (A6)$$

The resonance condition is written as follows:

$$\omega^2 = \omega_e(\omega_e - \omega_k + \omega_m), \quad (A7)$$

$$\omega_k = \gamma H_k. \quad (A8)$$

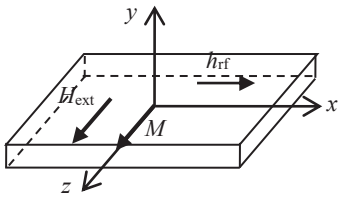

Fig.A-1
Without anisotropy
$N_x = N_z = 0$, $N_y = 1$

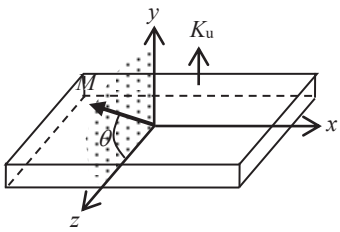

Fig.A-2
With perpendicular anisotropy
$N_x = N_z = 0$,
$N_{ye} = 1 - H_k/4\pi M_s$

When the perpendicular anisotropy is induced, the resonance frequency decreases.

Acknowledgements This work has been funded by the Japan Society for the Promotion of Science (JSPS) KAKENHI under Grand-in-aid No. 17H03385 and 18H05936. We are grateful to Dr. Miyazaki of Tohoku University for his kind support to TEM observation. We thank Prof. M. Yamaguchi of Tohoku University, and Dr. M. Naoe of Research Institute for Electro-magnetic materials, for their useful discussions and supportive advices. We wish to thank Mr. T. Hotchi, Mr. S. Motomura, Mr. S. Yamasaki, and Dr. M. Taguchi of KEYCOM corp. for his kind assistant and useful experimental suggestions. The authors would like to thank Enago for the English language review.

References

1) S. Takeda, T. Hotchi, S. Motomura, and H. Suzuki: *J. Magn. Soc. Jpn.*, **39**, 227 (2015).
2) S. Takeda and M. Naoe: *J. Magn. Magn. Mater,* **449**, 530 (2018).
3) W. B. Weir: *Proc. IEE*E, **62**, 1, 33 (1974).
4) A. M. Nicolson: *IEEE. Trans. Instrum. Meas.* **IM-17**, 395 (1968).
5) H. Kijima, S. Ohnuma, H. Masumoto: *J. Magn. Soc. Jpn.*, **36**, 287 (2012).
6) H. Kijima, Y. Zhang, N. Kobayashi, S. Ohnuma, H. Masumoto: *IEEE. Trans. Magn.*, **48,** 2910 (2012).
7) M. Naoe, N. Kobayashi, S. Ohnuma, M. Watanabe, T. Iwasa, and H. Masumoto: *IEEE Magn., Lett.*, **5**, #3700404 (2014).
8) H. Kijima-Aoki, S. Takeda, S. Ohnuma, and H. Masumoto: *IEEE Magn., Lett.*, **9**, #3704205 (2018).
9) S. Takeda, S. Motomura, T. Hotch, and H. Suzuki: *J. Magn. Soc. Jpn.*, **39**, 116 (2015).
10) S. Takeda and H. Suzuki: *J. Magn. Soc. Jpn.*, **33**, 171 (2009).
11) S. Takeda, S. Motomura, T. Hotch, and H. Suzuki: *J. Jpn. Soc. of Powder and Powder Metallurgy,* **61**, S1, S303 (2014).
12) D. M. Pozar: "Microwave Engineering 2nd ed.," *John Wiley & Sons, Inc.*, p.144 (1998).
13) C. Kittel: *Phys. Rev.* **73**, 2, 155 (1948).
14) J. Smit H.P.J. Wijn: "Ferrites," *Philips Technical Library*, p.83 (1965).

Received Mar. 4, 2019; Revised June 10, 2019; Accepted July 9, 2019,

J. Magn. Soc. Jpn., **43**, 99-104 (2019)

<Paper>

Heating Performance of Soft-heating Element with LC-booster for Invasive Hyperthermia Therapy

T. Takura, S. Kajiwara, H. Kikuchi, and H. Matsuki*

Tohoku Institute of Technology, *35-1 Yagiyama, Kasumicho, Taihaku-ku, Sendai 982-8577, Japan*

*New Industry Creation Hatchery Center, Tohoku University, *Aramaki, Aoba, 6-6-10, Aoba-ku, Sendai 980-8579, Japan*

The soft-heating method is an implantable hyperthermia method that can control the ultimate temperature of heating elements by using the Curie temperature of the magnetic material used in the element. It is a safe heating method. High heat generation has been achieved for heating elements by forming a metal ring around a core made of a ferrite-based magnetic material having a low Curie temperature. However, to generate a magnetic flux for heating deep inside the body, an exciting coil with a high withstand voltage and large allowable current has been required. In this research, we reduce the load on the exciting system, by developing a novel heating element using the LC-booster method. This wireless power transfer technology is excellent in matching with the load resistance and is proposed as a method for improving the performance of the heating element itself. Our proposed LC-booster method has better heat generation performance than the conventional methods. In addition, we prove that the performance could be improved by increasing the resonant frequency.

Key words: hyperthermia, soft-heating method, Curie temperature, wireless power transfer, LC-booster

1. Introduction

In recent years, many effective treatment methods have been proposed for cancer. However, the early detection of cancer is critical because it dramatically improves the survival rates after treatment. In deep cancer, often an important visceral organ is affected; therefore, extensive excision not only leads to the loss of function but also increases the risk of death. In the case of deep areas, physical access for frequent surgical treatment becomes complicated. To reduce the burden on the patients, we need local treatment that can preserve function.

Implantable hyperthermia is very effective for local treatment. One embedded hyperthermia method is the soft-heating method [1], which uses a heating element that combines a metal ring with a magnetic material of the Low Curie temperature. The soft-heating method uses a functional heating element that can control the short-circuit current flowing in the metal ring in a high-frequency magnetic field by using the Curie temperature of the magnetic material. As a result, the ultimate temperature of the element can be controlled. In other words, there is no need to adjust the output of the power source in the exciting system according to the temperature. Furthermore, by using a magnetic material with a Curie temperature higher than 42.5 °C, which is a typical treatment temperature for hyperthermia, the heating area can be expanded and the tumor tissue completely necrotized. Therefore, the risk of growing again can be reduced. It is similar to radiofrequency ablation (RFA) in that the heater temperature needs to be raised to 42.5 °C or higher. However, unlike RFA, the temperature of the heating element in the soft-heating method can be kept constant as described above; therefore, a cooling system is not necessary to prevent overheating. In [2], we confirmed that by using this method, a high therapeutic effect can be expected from the relationship between the progress of the tumor and the treatment conditions when a heat-generating element was inserted into a mouse's B16 melanoma [2]. For this, we required an excitation frequency of 200 kHz and a magnetic flux density of 3 mT. It is not easy to realize this condition deep inside the body. However, if we could improve the heat generation capacity of the heat-generating element, it would be possible to alleviate the excitation conditions, and we could facilitate the miniaturization and high functionality of the exciting apparatus. Therefore, in this research, to improve the heating capability of the heating element, we generate sufficient heat from the heating element even in low magnetic flux density by incorporating the LC-booster method [3], which has been established as the wireless power transfer (WPT) technology. The purpose of this study is to fabricate a prototype heating element that incorporates the LC-booster method, which is more efficient than the conventional methods. We did this by measuring the frequency characteristics of the input power and the temperature characteristics in a high-frequency magnetic field.

2. Configuration of Heating Element

2.1 Conventional type

Fig. 1 shows the equivalent circuit of a conventional heating element. L_1 is the inductance of the exciting coil; L_2 is the inductance of the metal ring; r_1 is the equivalent series resistance (ESR) of the exciting coil; r_2 is ESR of the metal ring; and M_{12} is the mutual inductance between them. The size of our element is largely different from the size of the exciting coil; therefore, M_{12} is very small. Under this low coupling

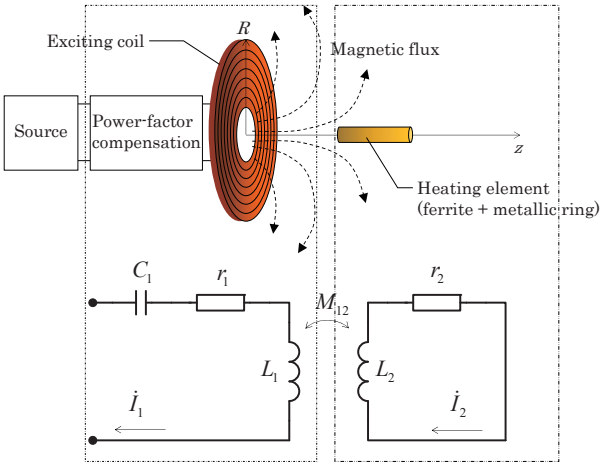

Fig. 1 Schematics of exciting part and heating element (conventional type).

condition, by keeping the current of the exciting coil constant, the induced voltage of the metal ring of the heating element can be made constant, and the heat output P can be stabilized. We assume that the current of the exciting coil is I_1, then P can be written as follows:

$$P = \frac{\omega^2 r_2 M_{12}^2}{r_2^2 + \omega^2 L_2^2} \left| \dot{I}_1 \right|^2 \tag{1}$$

Here, ω is the angular frequency. Therefore, it is possible to improve P by applying the magnetic flux density from the outside without changing the element structure. Also, from (1), when r_2 is regarded as a variable, P becomes the maximum when Q_2 is 1. As a method for realizing it, [4] proposed a method for adjusting the resistance by changing the thickness of the metal ring. We conducted the above animal experiments under the exciting condition (200 kHz, 3 mT) by using a heating element whose metal ring thickness had been optimally adjusted. We estimated the specifications about the coil for realizing this exciting condition in the deep part of the body (approximately 60 mm). The exciting coil assumes a spiral shape with one end at the center of the circle and the other end at the circumference. We assume that the coil radius is R, and the magnetic flux density in the z-axis direction is B_z. At a position vertically separated from the coil center by z, B_z is given as follows [5]:

$$B_z = \frac{\mu_0 NI}{2R} \left(\ln \frac{R + \sqrt{R^2 + z^2}}{z} - \frac{R}{\sqrt{R^2 + z^2}} \right) \tag{2}$$

Let us assume that R is 150 mm and z is 60 mm, and the magneto motive force NI required for B_z to be 3 mT is approximately 1000 AT. If the number of turns is 10, a current of 100 A is required. It is difficult to develop enough power supply unit for the specification. Therefore, it is essential to improve the performance of the heating element to miniaturize the exciting system.

2.2 LC-booster type

To solve the above problems, we propose a method that incorporates the LC-booster (a WPT technology) in a heating element. In WPT, the LC-booster system can change the magnetic field distribution near the load coil by incorporating an LC resonator between the transmitting and receiving coils and improving the efficiency at a specific load. Energy can be efficiently sent to the load; therefore, the heat output of the heating element may be improved. Fig. 2 shows a schematic diagram of the heating element and the equivalent circuit when the LC-booster system is incorporated. The difference from the WPT case is that the load resistance is shorted to form a one-turn metal ring, and the other points are the same. Using similar studies, researchers have proposed a method in which the LC resonant circuit itself is heated by using the RF/micro band electromagnetic field [6] [7]. The temperature needs to be constantly monitored because the temperature reached depends on the thermal equilibrium determined between the electromagnetic wave output and the surrounding environment. However, the structure proposed in this research does not require any temperature measurements because the ultimate temperature is determined in principle by the Curie temperature, and heat generation and temperature control are simultaneously realized by the hybrid heating structure of the LC resonant circuit and the metal ring. In this circuit configuration, the currents of LC-booster part and the metal ring cause a change in the magnetic flux density inside the core. The change can affect the core loss and the loss at the coil and the metal ring. In this study, the loss is equal to the heating performance. Therefore, it is important to evaluate the loss of the heating elements with different configuration (in this study, core only, conventional type, LC-resonator type, and LC-booster type).

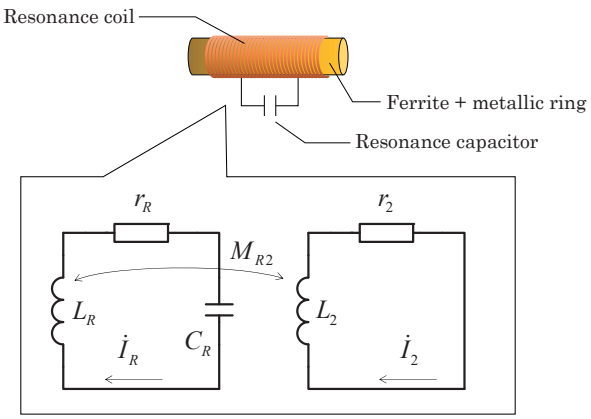

Fig. 2 Schematics of heating element (LC-booster type).

3. Evaluation of Heating Performance

3.1 Heating elements

We actually manufactured the four heating elements in order to confirm the heating performance. Fig. 3 shows the heater elements, and Table 1 shows the specifications of the elements. The magnetic material used was NP22D, a Ni-Zn ferrite manufactured by Hitachi Metals (see Table 2 for specifications). The metal ring was constructed by winding a conductive copper foil adhesive tape (TERAOKA 8315 0.05, copper foil thickness 0.018 mm) around the ferrite material. In addition, the resonator coil was constructed by winding the polyurethane copper wire (diameter 0.08 mm) 100 times on the metal ring. The board was connected at the end of the lead wire 100 mm from the heating element so that the resonator capacitor (film capacitor) could be easily replaced. First, the heating capacity was estimated by measuring the input power characteristics by using the prototype heating element.

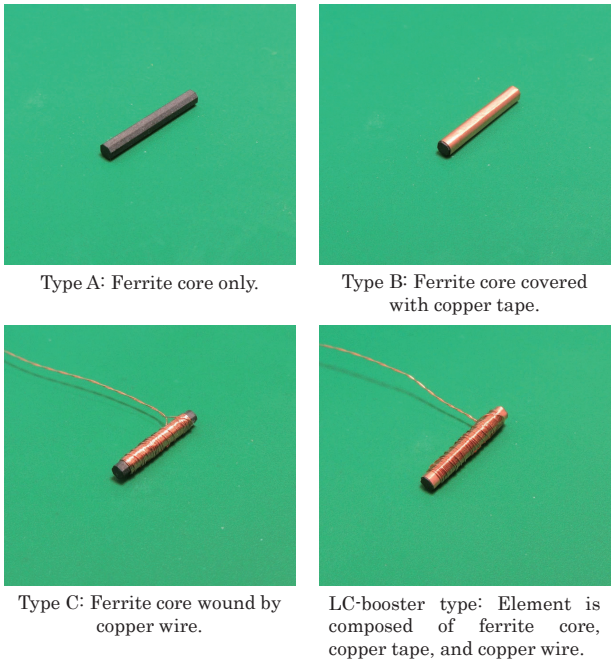

Type A: Ferrite core only.

Type B: Ferrite core covered with copper tape.

Type C: Ferrite core wound by copper wire.

LC-booster type: Element is composed of ferrite core, copper tape, and copper wire.

Fig. 3 Heating elements for experiment.

Table 1 Specifications of heating elements.

Type	A	B	C	LC-booster
Core	○	○	○	○
Copper foil	—	○	—	○
Coil	—	—	○	○

Table 2 Specifications of ferrite core.

Item	Value
Length [mm]	10
Width [mm]	1.2
Shape	Octagonal prism
Curie temperature [°C]	90
Initial permeability	2200

3.2 Experimental method

The input power P_{in} (active power) to the exciting coil consists of the power consumption P_1 of the exciting coil, the core loss P_c, the power consumption P_R in the LC-booster part, and the power consumption P_2 in the metal ring part. If we assume that the current I_1 of the exciting coil is constant, then the P_{in} to the exciting coil without any heating elements is equal to P_1. We have assumed that P_1 is also constant if I_1 is constant; therefore, the power consumption of the heating element can be obtained by subtracting P_1 from the input power when the heating element is disposed in the exciting coil. Therefore, the power consumption P of the entire heating element can be obtained from the following equation.

$$P = P_c + P_R + P_2 = P_{in} - P_1 \tag{3}$$

However, the existing exciting coil is much larger than the heating element; therefore, the coupling is low and it is not easy to measure the changes in the input power. Therefore, by using a small solenoid coil close to the heating element size, it is possible to evaluate the relative performances between the different heating elements by enhancing the coupling to raise the measurement sensitivity. The experimental environment is shown in Fig. 4. The small solenoid coil used in the experiment was 40 mm in length and 32 mm in diameter. There were 17 turns. P_{in} is obtained from the ESR r (measured using an LCR meter (Agilent E4980A)) and the current I (from the LCR meter) as follows:

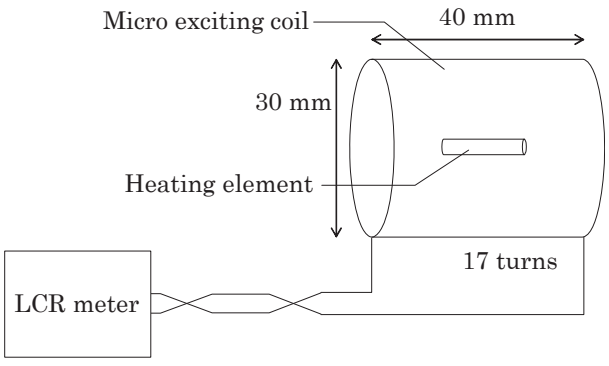

Fig. 4 Experimental circuit (for Type C and LC-booster type, resonance capacitor is outside micro exciting coil).

$$P_{in} = rI^2 \tag{4}$$

The heating elements used in the experiment are the four elements shown in Fig. 3. The capacitance value of the capacitor connected to Type C is 36.8 nF. (Hereinafter, the capacitance value mentioned will be the indicated value, not the measured value.) The capacitance value of the capacitor connected to the LC-booster type was the same as that of the capacitor connected to the Type C element. P_{in} was measured by changing the frequency from 20 kHz to 900 kHz. In this study, to clarify the characteristics of the heater with almost the same shape, the types of core material, copper foil and wire material are not changed.

3.3 Comparison of heating performance

Fig. 5 shows the measurement results of the frequency characteristics of the power consumption of the heating element. In Type A, it was confirmed that P rises in the high-frequency band, but it was a much smaller value than other heating elements. P is considered to be almost equal to P_c at this time, the core loss contributed less to the performance of the heating element. In Type B, P increased with the increase in frequency. However, in the Type C and the LC-booster type elements, P increased rapidly at a specific frequency. In particular, the highest value was Type C. As compared with the LC-booster type, Type C showed a high Q factor. In other words, the effective frequency band was narrow. Therefore, we assume that Type C is susceptible to capacitance changes in the connected capacitor; these changes include variations in the capacitors, the molds of the heating elements, and the in-vivo permittivity. However, although P is lower in the LC-booster method than that in Type C, the usable band was wide. Therefore, the LC-booster type was less susceptible to capacitance changes. To confirm the characteristics, we measured P when the capacitance of the connected capacitor was increased without changing the frequency. The results are shown in Fig. 6. In Type C, an increase in the capacitance by approximately 9% caused P to decay to 40% of its value before the increase. However, the rate of the LC-booster type was 92%. It is possible for the LC-booster type to maintain the performance if a capacitance change occurs. Therefore, the LC-booster type heating element is suitable for practical purpose.

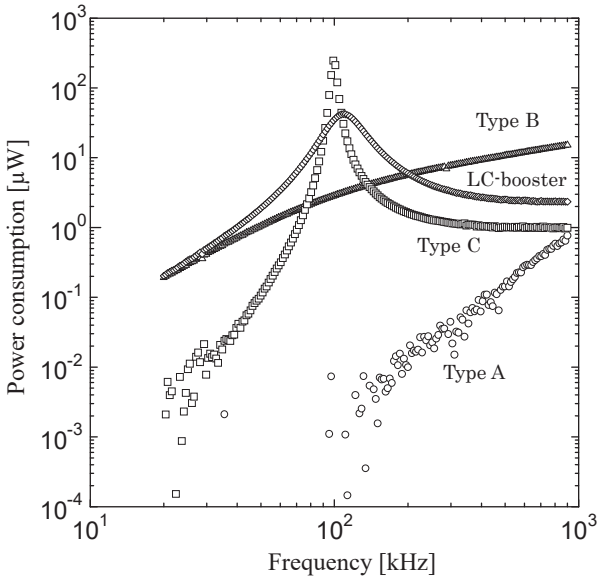

Fig. 5 Frequency characteristics of power consumption of heating element.

Next, to clarify the influence of increasing the resonant frequency on the heat generation performance, we considered the relationship between the maximum power consumption and the frequency by changing the capacitance of the connected capacitor. The results are shown in Fig. 7. At this time, the capacitance values of the capacitors used were 6.8, 10, 16.8, and 36.8 nF. Within the measured range, the maximum power consumption increased almost in proportion to the frequency. In other words, increasing the resonance frequency leads to better performance.

4. Heating Experiment

4.1 Experimental implementation

The power that could be supplied from the LCR meter (used in the previous section) was very small; therefore, it was not possible to heat the LC-booster type heating element to observe the temperature rise. Therefore, in this section, by using the exciting coil and the high-frequency power source (which can realize large exciting conditions), we clarify the performance of the LC-booster type element from the temperature characteristic by changing the applied magnetic flux density and the resonance condition. A schematic diagram of the experiment is shown in Fig. 8. In the experiment, we used Helmholtz-type coils for the exciting coil, and the heating element was placed at the

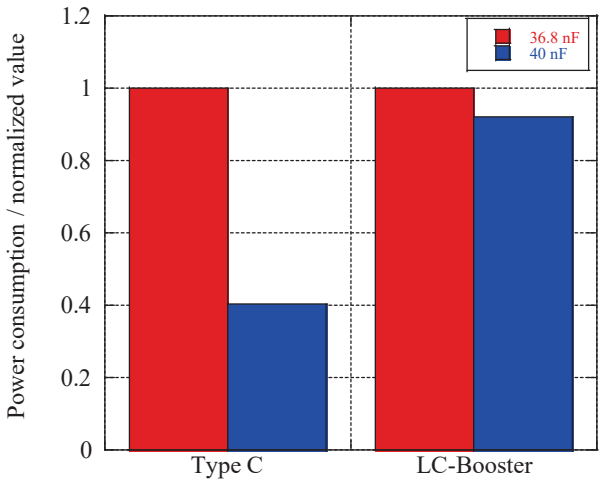

Fig. 6 Attenuation of power consumption due to capacity change. Frequency of Type C is 98.9 kHz, and that of LC-booster is 108.8 kHz.

center between the coils. A heat insulating material was used to eliminate the influence of the heat generation of the exciting coil. A fiber optical thermometer (Anritsu Meter FL-2000) was used to measure the temperature, and the measurement time was 300 s. Note that this experiment was conducted at room temperature.

4.2 Temperature profiles for changing magnetic flux densities

Fig. 9 shows the temperature profile when the magnetic flux density was changed to 0.5, 1, 2, and 3 mT. At this time, the exciting frequency was 102 kHz, and the heating elements used were the conventional Type B and the LC-booster type (36.8 nF). We selected an exciting frequency slightly different from the frequency shown in Fig. 7 to consider the allowable current of the capacitor. As a result, the ultimate temperature reached its maximum at an applied magnetic flux density of 3 mT in both cases: 84.9 °C for Type B and 86.2 °C for the LC-booster type. There was no significant difference in the ultimate temperature, and the temperature could be controlled near the Curie temperature. In other words, the LC resonator does not continue to generate heat beyond the Curie temperature. Moreover, when the condition of the magnetic flux density was lowered, the temperature difference after 300 s of the two began to increase, and the temperature difference became approximately 30 °C at 1 mT. This result is similar to the results given in Section 3.3 and shows that the LC-booster type element has better performance than the conventional elements. Therefore, by adopting the LC-booster method, it is possible to

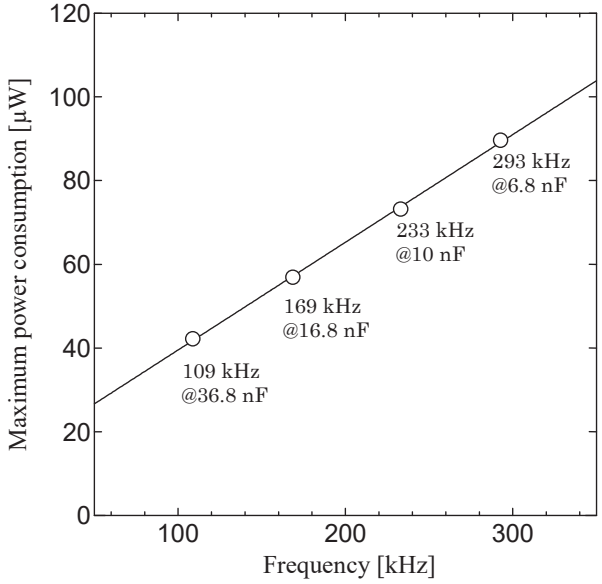

Fig. 7 Transition of maximum power consumption in LC-booster type element.

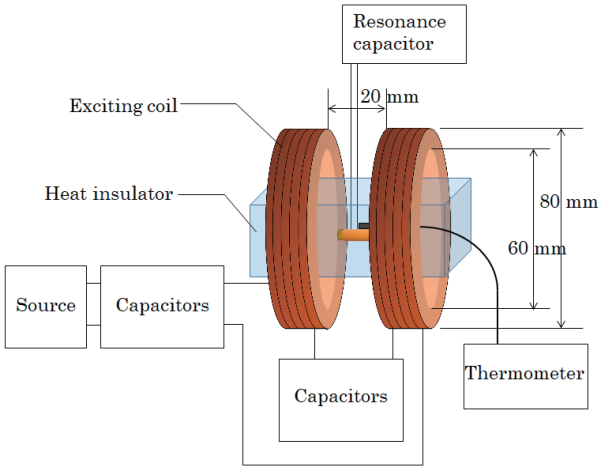

Fig. 8 Experimental schematic diagram for measuring temperature profile.

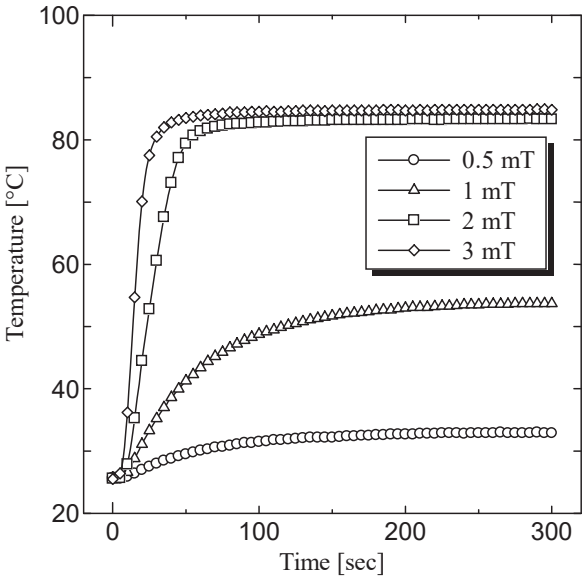

(a) Conventional type (type B).

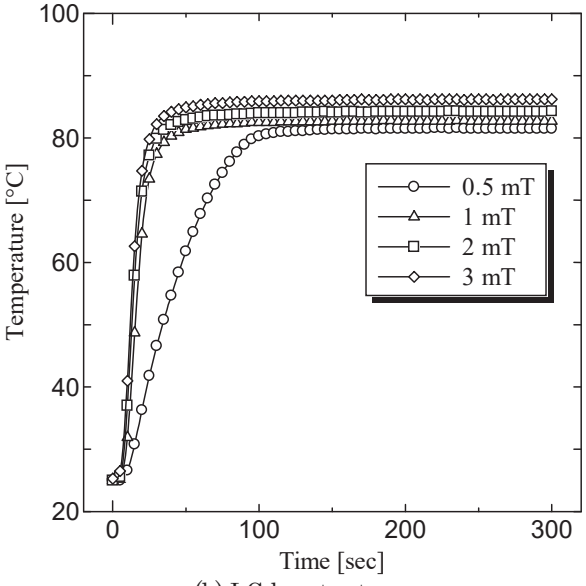

(b) LC-booster type.

Fig. 9 Temperature profiles of conventional and LC-booster type elements in high frequency magnetic field.

improve the heat output of the conventional heating element without losing the temperature controllability.

4.3 Effect of high resonance frequency

In Section 3.3, we suggested that performance can be improved by setting the LC-booster type element to a high resonance frequency. Therefore, in this section, we confirm the temperature characteristics by changing the resonance frequency setting for a constant applied magnetic flux density. In the experiment, the capacitance value of the capacitor connected to the LC-booster type was the same as that in Fig. 7, and the capacitor connected to the exciting coil was adjusted so that the exciting frequency approached the frequencies shown in Fig. 7. The measured results are shown in Fig. 10. At this time, the applied magnetic flux density was fixed at 0.5 mT. As a result, by increasing the frequency, the slope of the initial temperature rise became large, and the temperature characteristics under the low magnetic flux density condition of 0.5 mT were improved. The capacitance value of the connected capacitor could be reduced as the resonant frequency was increased. In other words, the volume of the entire heating element can be reduced, which leads to high heat generation.

5. Conclusion

In this paper, we fabricated an LC-booster type heating element, and we evaluated its performance from the frequency characteristics of the input power and the temperature characteristics in a high-frequency magnetic field. As a result, the LC-booster method achieved higher heat generation than the conventional method, and the LC-booster method could maintain temperature controllability. In addition, the LC-booster method has a wider band than the method that uses only the LC resonator. The LC-booster method is not susceptible to capacitance changes and generates stable heat. Furthermore, heat generation can be improved and the volume can be reduced by increasing the resonance frequency.

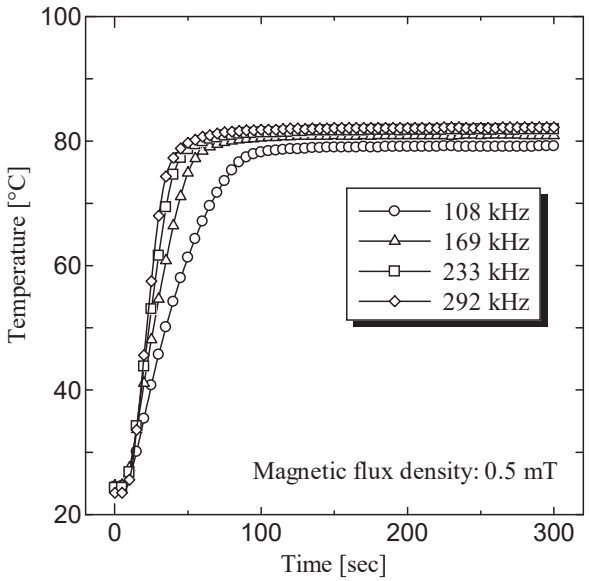

Fig. 10 Temperature profiles with changing resonance frequencies in LC-booster type element.

Acknowledgements This work was supported by JSPS KAKENHI Grant Number 17K13038

References

1) H. Matsuki: *Seitai Denji Kogaku Gairon* (in Japanese), pp.121-128 (Coronasya, Tokyo, 1999).
2) T. Takura, F. Sato, H. Matsuki, T. Fujimura, S. Aiba, and T. Sato: *J. Magn. Soc. Jpn.*, **32**, 439 (2008).
3) T. Takura, T. Misawa, F. Sato, T. Sato, and H. Matsuki: *J. Magn. Soc. Jpn.*, **37**, 102 (2013).
4) T. Takura, T. Maruyama, F. Sato, H. Matsuki, S. Aiba, and T. Sato: *J. Magn. Soc. Jpn.*, **31**, 288 (2007).
5) K. Goto and S. Yamazaki: *Shoukai Denjikigaku Enshu* (in Japanese), p.241 (Kyoritsu Shuppan, Tokyo, 1970).
6) Y. Kotsuka, K. Orii, H. Kojima, and M. Tanaka: *IEEE Trans. MTT.*, **47**, pp. 2630-2635 (1999).
7) M. Shimizu, T. Yamada, Y. Takemura, T. Niwa, and T. Inoue: *J. Magn. Soc. Jpn.*, **34**, 449 (2010).

Received May. 09, 2019; Accepted June. 27, 2019

Journal of the Magnetics Society of Japan

Vol. 43 No. 5 (通巻第 305号) 2019年 9 月 1 日発行

Vol. 43 No. 5 Published Sep. 1, 2019
by the Magnetics Society of Japan
Tokyo YWCA building Rm207, 1–8–11 Kanda surugadai, Chiyoda-ku, Tokyo 101–0062
Tel. +81–3–5281–0106 Fax. +81–3–5281–0107

Printed by JP Corporation Co., Ltd.
Sports Plaza building 401, 2–4–3, Shinkamata Ota-ku, Tokyo 144–0054
Advertising agency: Kagaku Gijutsu-sha

発行：（公社）日本磁気学会 101–0062 東京都千代田区神田駿河台 1–8–11 東京YWCA会館 207 号室
製作：ジェイピーシー 144–0054 東京都大田区新蒲田 2–4–3 スポーツプラザビル401 Tel.（03）6715–7915
広告取扱い：科学技術社 111–0052 東京都台東区柳橋 2–10–8 武田ビル 4F Tel.（03）5809–1132